Generation of Greenberger-Horne-Zeilinger states for silicon-vacancy centers using a decoherence-free subspace

Yi-Fan Qiao,[1] Jia-Qiang Chen,[1] Xing-Liang Dong,[1] Bo-Long Wang,[1] Xin-Lei Hei,[1]
Cai-Peng Shen,[1] Yuan Zhou,[2] and Peng-Bo Li [1,*]

[1]*Ministry of Education Key Laboratory for Nonequilibrium Synthesis and Modulation of Condensed Matter, Shaanxi Province Key Laboratory of Quantum Information and Quantum Optoelectronic Devices, School of Physics, Xi'an Jiaotong University, Xi'an 710049, China*
[2]*School of Science, Hubei University of Automotive Technology, Shiyan 442002, China*

Generating Greenberger-Horne-Zeilinger (GHZ) states of solid-state spins is of great significance for quantum metrology and quantum error correction. We propose here an efficient scheme for generating high fidelity GHZ states in a solid-state setup where multiple silicon-vacancy (SiV) centers are embedded in a quasi-one-dimensional acoustic diamond waveguide. The lattice distortion gives rise to a strong strain coupling between the orbital degree of freedom of SiV centers and the continuum phonon modes. Due to the permutation symmetry, we can take advantage of the decoherence-free subspace to avoid dissipation. Under the quantum Zeno regime, two control fields are used to achieve a ladderlike coupling structure in decoherence-free subspace along with an off-resonant two-photon Raman transition process. We calculate the pulse sequences for $N = 4$ and at the same time analyze the effect of different collective decay rates. Moreover, we consider the disorder in the imperfect position of SiV centers and the inhomogeneous strain coupling. This paper may provide a feasible protocol for the generation of GHZ states in a solid-state system.

I. INTRODUCTION

Entanglement is one of the most remarkable and significant characteristics of quantum physics, which has become a main resource for various quantum technology tasks including quantum information processing [1–3], quantum communication [4,5], and quantum cryptography [6–8]. Besides, entanglement has also provided new insights for understanding other phenomena, such as superradiance [9,10] and superconductivity [11]. For these reasons, great effort has been devoted to preparing various multipartite entangled states over the past few years [12–23]. In particular, the Greenberger-Horne-Zeilinger (GHZ) state [24–26] has attracted much attention for its potential applications ranging from quantum metrology [27–31] to quantum error correction [32,33]. So far, such states have been generated experimentally involving superconducting qubits [34,35] and Rydberg atoms [36]. Despite these impressive progresses, generating high fidelity GHZ states with multiple qubits still remains challenging. To achieve this goal, several schemes have been proposed based on the Ising model [17,37,38], Bose-Hubbard model, and one-axis twisting model with Rydberg atoms [37,39], ultracold atoms [20], and trapped ions [40], respectively.

Recently, the silicon-vacancy (SiV) center has [41–50] composed a promising platform to generate entangled states of solid-state spins. Due to the inversion symmetry, the negatively charged SiV center in diamond presents strong zero-phonon line emission, narrow inhomogeneous broadening, as well as stable optical transition frequencies [51–57]. Furthermore, it is demonstrated that the coherence time of the SiV center has been improved to ∼10 ms at 100-mK temperature [58]. However, the coupling between SiV centers and the external environment or bath will inevitably induce decoherence, which causes information loss from the SiV centers to the environment by means of dephasing or dissipation, and, thus, affects the realization of quantum information processing. Much effort has been devoted to protecting the system from the effect of decoherence, and various strategies have already been proposed so far. Among them, a promising solution to avoid decoherence in quantum information processing is to encode quantum information in decoherence-free subspace (DFS) [59–67], over which the evolution of the states is unitary and robust against noncollective perturbation as well. A crucial characteristic of the existence of DFS is the dynamic symmetry [68–71], i.e., the coupling between the SiV center and the environment possesses permutation symmetry, which gives rises to collective decoherence.

In this paper, we propose an efficient scheme to generate the GHZ state in a hybrid quantum system, where an array of $N + 1$ SiV centers are embedded in a one-dimensional (1D) phononic diamond waveguide. As an auxiliary, the $(N + 1)$th SiV center far right of the waveguide needs to be addressed individually in this scheme. The electronic ground state of SiV centers has a strong strain coupling between its orbital degree of freedom and the phonon modes of the waveguide [72]. As the instinct feature of the solid waveguide, we can modulate the phase difference by choosing the position of the SiV centers [73,74]. Particularly, when the distances

_____
*lipengbo@mail.xjtu.edu.cn

between the centers equal to the integer multiples of the phonon wavelength, the dipole-dipole interaction can be switched off due to the destructive interference, thus, realizing a Dicke superradiance model [73]. Due to the permutation symmetry, there exists a special DFS in which the states are immune to decoherence [59]. We here need to apply two control fields: One allows to control the ancilla center independently, and the other needs to control all of SiV centers, which can ensure an off-resonant two-photon transition process in DFS. We can generate the GHZ state by alternating between the two-photon Raman transition and the control field of ancilla center. We give the pulse sequences for the ideal case and analyze the errors that may occur within each step. We also simulate the fidelity of the target GHZ state. This scheme provides a promising and convenient avenue for the generation of high fidelity GHZ states.

II. MODEL

We consider a chain of N SiV centers plus an individual ancillary SiV center equally spaced in a 1D phononic waveguide at position x_n ($n = 1, 2, \ldots, N, N + 1$), as depicted in Fig. 1(a). The electronic ground states of SiV centers as a result of the lattice distortion, permit a direct and strong strain coupling to the continuum phonon modes. In addition, we can apply the classical optical fields to drive the transitions between the ground states and the excited states resonantly or near resonantly.
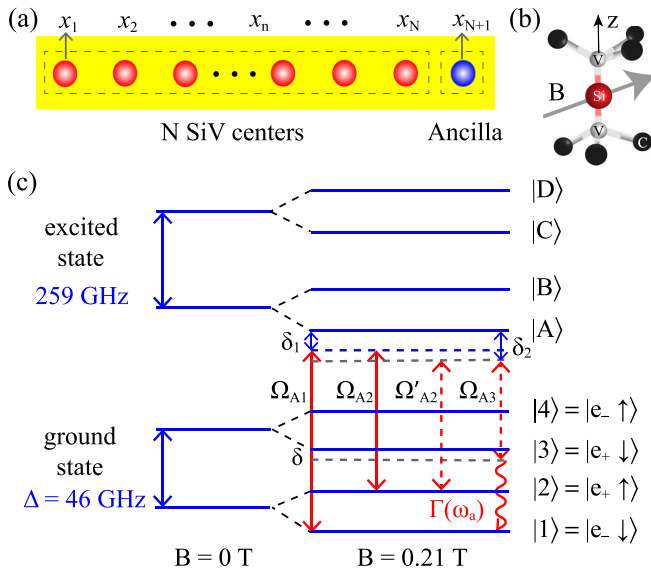

FIG. 1. (a) Sketch of an array of N SiV centers plus one ancilla center embedded in a 1D phononic waveguide at fixed positions x_n. The distance between two arbitrary adjacent SiV centers are the same. The length, width, and thickness of the waveguide are L, w, and t, respectively. (b) Atomic structure of the SiV color center in diamond. The external magnetic field is tilted from the symmetry axis of SiV centers with an angle of 70.5°. (c) Electronic level scheme of the SiV center at $B = 0$ and $B = 0.21$ T. Optical Raman driving schemes: the transition between $|1\rangle \leftrightarrow |2\rangle$ is realized by making use of excited-state $|A\rangle$ with amplitudes Ω_{A1}, Ω_{A2}, and detuning δ_1. Another two optical drivings with amplitudes Ω'_{A2}, Ω_{A3}, and detuning δ_2, realize the transition between $|2\rangle \leftrightarrow |3\rangle$.

A. Hamiltonian

The silicon-vacancy center consists of a silicon atom and a split vacancy replacing two neighboring carbon atoms, displayed in Fig. 1(b). In the absence of external magnetic fields, the energy levels are featured by orbitally split ground and excited states [56], i.e., $|e_+ \downarrow\rangle$, $|e_- \uparrow\rangle$ and $|e_+ \uparrow\rangle$, $|e_- \downarrow\rangle$, with a separation of $\Delta = 46$ GHz between the two branches of ground states. Here $|e_\pm\rangle$ are the eigenstates of the angular momentum operator, and the up (or down) arrow denotes the spin-up (or spin-down) state of the spin projections, respectively [41,42]. In the presence of external magnetic-fields $\vec{B}$, the spin degeneracy is lifted, and its ground and excited states can be characterized by fourfold states $|s\rangle$ due to the Zeeman effect [Fig. 1(c)] with $s = 1$–4 for ground states and $s = A, B, C, D$ for excited states. We take the fourfold ground states and a single excited state $|A\rangle$ into our consideration, and the Hamiltonian of SiV centers reads (we set $\hbar = 1$)

$$\hat{H}_{\mathrm{SiV}} = \sum_{n}^{N+1} \left(\sum_{s} \omega_s |s\rangle_n \langle s| + \omega_A |A\rangle_n \langle A| \right). \quad (1)$$

Here, ω_s and ω_A are the energies of the ground-states $|s\rangle$ and excited state $|A\rangle$, and the symbol n denotes the nth SiV center at the position $\vec{r}_n = (x_n, y_n, z_n)$. The quantized Hamiltonian of phonon modes is described by

$$\hat{H}_{\mathrm{B}} = \sum_{j,k} \omega_{j,k} \hat{a}^\dagger_{j,k} \hat{a}_{j,k}, \quad (2)$$

where $\hat{a}^\dagger_{j,k}$ ($\hat{a}_{j,k}$) is the bosonic creation (annihilation) operator of the kth mode of the jth branch at frequency of $\omega_{j,k}$. In addition, the lattice distortion of longitudinal compression modes affects the electronic structure of the defect, which gives rise to strain coupling between the phonons and the orbital degrees of freedom of the SiV centers. When considering the small displacement of the defect atoms, the coupling between the phonon modes and the orbital degrees of freedom is linear in the Born-Oppenheimer approximation [53,72,75]. In this case, the strain interaction is given by

$$\hat{H}_{\mathrm{SB}} = \sum_{n,j,k} g^n_{j,k} \hat{a}_{j,k} \hat{J}^n_+ e^{ikx_n} + \mathrm{H.c.} \quad (3)$$

Here, for the nth SiV spin, $\hat{J}_- = \hat{J}^\dagger_+ = |1\rangle\langle 3| + |2\rangle\langle 4|$ is the spin-conserving lowering operator, and the coupling strength is $g^n_{j,k} = d\sqrt{\hbar k^2 / 2\rho L A \omega_{j,k}} \xi_{j,k}(y_n, z_n)$ with the strain sensitivity $d/2\pi = 1$ PHz, the mass density ρ, the transverse area $A = wt$, and the length L of the waveguide, respectively. The dimensionless coupling profile $\xi_{j,k}(y_n, z_n)$, caused by the specific strain distribution, is approximately unity for the homogeneous compression mode.

B. Driving scheme

Note that the optical transitions between the ground and the excited states are spin conserving, that is, transitions can only be achieved between states with the same spin projections [42]. When the magnetic field is aligned with the SiV center symmetry axis, all states have the unity spin polarization; the transition between states with opposite spin projections are forbidden [42,55]. We further consider a

misalignment between the magnetic field and the SiV axis in which case all electronic states have both spin-up components and spin-down components. As a consequence, optical transitions between all levels are permitted. We here apply a magnetic field of 0.21 T at an angle of $70.5°$ with respect to the SiV symmetry axis [55]. In our scheme, we need to realize the transitions $|1\rangle \leftrightarrow |2\rangle$ ($|2\rangle \leftrightarrow |3\rangle$), and we can introduce the so-called Λ-type Raman processes to obtain these transitions effectively. As illustrated in Fig. 1(c), by using the laser fields to excite resonant transitions $|A\rangle \leftrightarrow |1\rangle$ and $|A\rangle \leftrightarrow |2\rangle$ ($|A\rangle \leftrightarrow |2\rangle$ and $|A\rangle \leftrightarrow |3\rangle$) simultaneously, we can deduce the Hamiltonian with the driving fields as

$$\hat{H}_{12} = \frac{\Omega_{A1}}{2}|1\rangle\langle A|e^{i\omega_{A1}t} + \frac{\Omega_{A2}}{2}|2\rangle\langle A|e^{i\omega_{A2}t} + \text{H.c.},$$

$$\hat{H}_{23} = \frac{\Omega'_{A2}}{2}|2\rangle\langle A|e^{i\omega'_{A2}t} + \frac{\Omega_{A3}}{2}|3\rangle\langle A|e^{i\omega_{A3}t} + \text{H.c.}, \quad (4)$$

where $\Omega_{As}(s = 1–3)$ and Ω'_{A2} are the tunable Rabi frequencies of the optical driving fields with the frequencies ω_{As} and ω'_{A2}, respectively. We assume that all of the fields are on the two-photon off-resonance in Raman transitions with $\delta_1 = \omega_A - \omega_1 - \omega_{A1} = \omega_A - \omega_2 - \omega_{A1}$ and $\delta_2 = \omega_A - \omega_2 - \omega'_{A2} = \omega_A - \omega_3 - \omega_{A3} + \delta$. In the condition of $\delta_1 \gg \Omega_{A1}, \Omega_{A2}$ and $\delta_2 \gg \delta, \Omega'_{A2}, \Omega_{A3}$, the effective driving Hamiltonian can be written as

$$\hat{H}_{12}^{\text{eff}} = \frac{\Omega_1}{2}|2\rangle\langle 1| + \text{H.c.},$$

$$\hat{H}_{23}^{\text{eff}} = \frac{\Omega_2}{2}|3\rangle\langle 2| + \text{H.c.} + \delta|3\rangle\langle 3|, \quad (5)$$

with the effective Rabi frequencies $\Omega_1 = -\Omega_{A1}^*\Omega_{A2}/2\delta_1$ and $\Omega_2 = -\Omega_{A3}\Omega_{A2}'^*(2\delta_2 - \delta)/4\delta_2(\delta_2 - \delta)$. Here, we ignore the additional Stark-shift terms, which can be compensated by engineering the detuning, and Eq. (5) is obtained in a rotating frame with the unitary operation $U = e^{-i\delta|3\rangle\langle 3|t}$. In our scheme, the ancillary center needs to be addressed individually, and the detuning for $(N + 1)$ SiV centers are all identical. The final effective control fields are given by

$$\hat{H}_{12}^{\text{C}} = \frac{\Omega_1}{2}\sigma_{21}^{N+1} + \text{H.c.},$$

$$\hat{H}_{23}^{\text{D}} = \left(\frac{\Omega_2}{2}\sum_{n=1}^{N}\sigma_{32}^n + \frac{\Omega_2'}{2}\sigma_{32}^{N+1} + \text{H.c.}\right) + \delta\sum_{n=1}^{N+1}\sigma_{33}^n, \quad (6)$$

where $\sigma_{ij}^n = |i\rangle_n\langle j|$.

C. Master equation

We define $\hat{\rho}$ as the density operator, which describes the SiV degrees of freedom. As the 1D waveguide has a much faster relaxation timescale than the SiV centers, we can eliminate the phononic modes in the limit of Born-Markov approximation and obtain an effective master equation [76] to present the dynamics of the SiV centers of the form $d\hat{\rho}/dt = \mathcal{L}[\hat{\rho}]$, with the superoperator,

$$\mathcal{L}[\hat{\rho}] = \sum_{n,m} G_{nm}(2\hat{\sigma}_-^n\hat{\rho}\hat{\sigma}_+^m - \hat{\sigma}_+^n\hat{\sigma}_-^m\hat{\rho} - \hat{\rho}\hat{\sigma}_+^n\hat{\sigma}_-^m). \quad (7)$$

Here we define the Pauli matrices $\sigma_-^n = |1\rangle_n\langle 3|$, $\sigma_+^n = |3\rangle_n\langle 1|$, and $G_{nm} = \frac{\Gamma}{2}e^{ik(\Delta)(x_n - x_m)}$ is the collective decay rate. $\Gamma =$

$\gamma(\Delta)$ characterizes the phonon-induced decay rate for the higher-energy orbital state $|3\rangle$ with $\gamma(\omega) = d^2\hbar\omega/(\rho A v^3)$ in a linear dispersion $\omega_k = vk$, where v is the group velocity and Δ is the energy difference between states $|1\rangle$ and $|3\rangle$. We precisely choose the position of the SiV centers such that $x_n = n\lambda_0 = 2n\pi/k(\Delta)$ ($n \in \mathbb{N}$), where $\lambda_0 \approx 200$ nm is the phonon wavelength, the coherent dipole-dipole interactions are eliminated due to the destructive interference [73,74,77], and Eq. (7) reduces to a pure Dicke superradiant decay described by

$$\dot{\rho} = \mathcal{L}_D[\hat{\rho}]$$
$$= \frac{\Gamma}{2}(2\hat{S}_-\hat{\rho}\hat{S}_+ - \hat{S}_+\hat{S}_-\hat{\rho} - \hat{\rho}\hat{S}_+\hat{S}_-), \quad (8)$$

where $\hat{S}_\pm = \sum_{n=1}^{N+1}\hat{\sigma}_\pm^n$ are the collective spin operators.

III. DECOHERENCE-FREE SUBSPACE

Decoherence arises from the instinctive coupling between quantum systems and the surrounding bath, and this detrimental factor leads to a nonunitary system dynamic evolution [61,78]. This effect is undesirable since it results in an inevitable decay of the coherent system. Fortunately, DFS [59–67,77] provides a powerful approach to preserve delicate quantum information from decoherence. The essential idea of DFS is to look for a special noiseless subspace of the full system Hilbert space. Several works have put forward various methods to create a DFS [78]. Here, we follow the method proposed in Ref. [77] to establish such a DFS in our model through the Lindblad master equation Eq. (8). It is obvious that the master equation separates the unitary and decoherence dynamics, and all of the nonunitary decoherence dynamics accounts for the Lindblad term $\mathcal{L}_D[\rho]$. Clearly, an intuitive DFS condition is supposed to vanish with the $\mathcal{L}_D[\rho]$ term, and the system, hence, will undergo a pure unitary evolution [77]. From this point, the necessary and sufficient conditions can be derived. Specifically, the DFS is made up of these states $|\psi\rangle$ satisfying

$$\hat{S}_-|\psi\rangle = 0. \quad (9)$$

These states can be easily described in the collective angular momentum basis $\{|J, m_J\rangle\}$, which is the eigenstates of the collective operators $\hat{S}^2$ and $\hat{S}_z$ with $J = N/2, N/2 - 1, \ldots, 0$ and $m_J = -J, -J + 1, \ldots, J$.

Subsequently, it is necessary to find out all the decoherence-free states from Eq. (9). Due to the high symmetry of those decoherence-free states, we make use of the following notation to describe arbitrary symmetric states over N centers:

$$|M_{\alpha,\beta}\rangle = \mathcal{N}(\alpha, \beta)^{-1/2}\text{sym}\{|2\rangle^{\otimes\alpha}$$
$$\otimes|3\rangle^{\otimes\beta} \otimes |1\rangle^{\otimes N-\alpha-\beta}\}, \quad (10)$$

where the multinomial coefficient $\mathcal{N}(\alpha, \beta) = \binom{N}{\alpha,\beta,N-\alpha-\beta}$ gives the normalization of these states [77]. This notation denotes that there are α centers at state $|2\rangle$, β centers at state $|3\rangle$, and the rest $N - \alpha - \beta$ centers at state $|1\rangle$. In addition, we use an individual notation $|s'\rangle_A$ to describe the ancilla center, where $s' = 1–3$ represent the three possible states of the ancilla center. Due to the collective spin operator $\hat{S}_-$ acts

on states $|1\rangle$ and $|2\rangle$ equal to zero, we can easily guess that all the superposition states of $|1\rangle$ and $|2\rangle$ of the $N + 1$ SiV centers are the possible decoherence-free states. We further consider the states including excited-state $|3\rangle$. One can find that for each α if and only if there is one center in excited-state $|3\rangle$ among the $N + 1$ SiV centers, the combination of the state $M_{\alpha,1}$ with the ancilla fulfilling the permutation symmetry belongs to DFS [77]. To summarize, these states are

$$|\Psi_1^\alpha\rangle = |M_{\alpha,0}\rangle \otimes |1\rangle_A,$$

$$|\Psi_2^\alpha\rangle = |M_{\alpha-1,0}\rangle \otimes |2\rangle_A,$$

$$|\Psi_3^\alpha\rangle = \sqrt{\frac{N_{\alpha+1}}{N_{\alpha+1} + 1}} |M_{\alpha,0}\rangle \otimes |3\rangle_A$$

$$- \sqrt{\frac{1}{N_{\alpha+1} + 1}} |M_{\alpha,1}\rangle \otimes |1\rangle_A, \quad (11)$$

where $N_\alpha = N - \alpha + 1$. Acting Hamiltonian $\hat{H}_{23}^D$ on the first two states, we have

$$\hat{H}_{23}^D |\Psi_1^\alpha\rangle = \frac{\Omega_2}{2} \sqrt{\alpha} |M_{\alpha-1,1}\rangle \otimes |1\rangle_A,$$

$$\hat{H}_{23}^D |\Psi_2^\alpha\rangle = \frac{\Omega_2}{2} \sqrt{\alpha - 1} |M_{\alpha-2,1}\rangle \otimes |2\rangle_A$$

$$+ \frac{\Omega_2'}{2} |M_{\alpha-1,0}\rangle \otimes |3\rangle_A. \quad (12)$$

By projecting the atomic state into the DFS, we obtain states $|\Psi_{1,2}^\alpha\rangle$ coupled with $|\Psi_3^\alpha\rangle$ as follows:

$$\hat{H}_{23}^D |\Psi_1^\alpha\rangle = -\frac{\Omega_2}{2} \sqrt{\frac{\alpha}{N_\alpha + 1}} |\Psi_3^{\alpha-1}\rangle + \frac{\Omega_2}{2} \sqrt{\frac{\alpha N_\alpha}{N_\alpha + 1}} |\chi_1^{\alpha-1}\rangle,$$

$$\hat{H}_{23}^D |\Psi_2^\alpha\rangle = \frac{\Omega_2'}{2} \sqrt{\frac{N_\alpha}{N_\alpha + 1}} |\Psi_3^{\alpha-1}\rangle + \frac{\Omega_2'}{2} \sqrt{\frac{1}{N_\alpha + 1}} |\chi_1^{\alpha-1}\rangle$$

$$+ \frac{\Omega_2}{2} \sqrt{\alpha - 1} |\chi_2^{\alpha-1}\rangle, \quad (13)$$

where two states $|\chi_1^{\alpha-1}\rangle = \sqrt{\frac{1}{N_{\alpha+1}}} |M_{\alpha-1,0}\rangle \otimes |3\rangle_A + \sqrt{\frac{N_\alpha}{N_{\alpha+1}}} |M_{\alpha-1,1}\rangle \otimes |1\rangle_A$ and $|\chi_2^{\alpha-1}\rangle = |M_{\alpha-2,1}\rangle \otimes |2\rangle_A$ are outside the DFS [77]. It is obvious that these two states show an enhanced decay rate $\Gamma_e = (N_\alpha + 1)\Gamma$ by acting the collective operator $\hat{S}_-$ on them [77]. Therefore, $|\chi_{1/2}^\alpha\rangle$s are only virtually populated so that we can neglect them. Thus, we can obtain an effective Λ scheme within the DFS via far-detuned state $|\Psi_3^\alpha\rangle$ with effective Raman intensities,

$$\Omega_{13}^\alpha = \langle\Psi_3^{\alpha-1}|\hat{H}_{23}^D|\Psi_1^\alpha\rangle = -\frac{\Omega_2}{2} \sqrt{\frac{\alpha}{N_\alpha + 1}},$$

$$\Omega_{23}^\alpha = \langle\Psi_3^{\alpha-1}|\hat{H}_{23}^D|\Psi_2^\alpha\rangle = \frac{\Omega_2'}{2} \sqrt{\frac{N_\alpha}{N_\alpha + 1}}. \quad (14)$$

We can realize an off-resonance two-photon transition by setting $|\Omega_{13}^\alpha| = |\Omega_{23}^\alpha|$, which yields $|\Omega_2'| = |\Omega_2|\sqrt{\alpha/N_\alpha}$. In the condition $\delta \gg \Omega_{13}^\alpha, \Omega_{23}^\alpha$, we can eliminate excited-state $|\Psi_3^\alpha\rangle$ and obtain the effective Hamiltonian for the αth
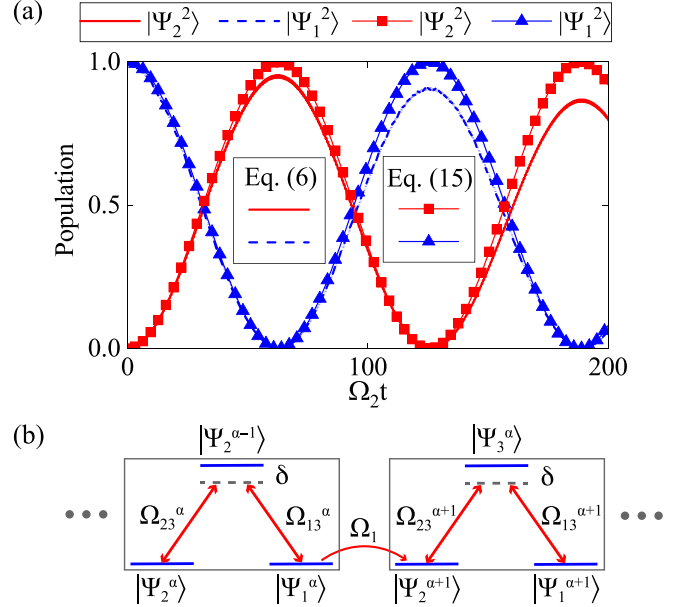

FIG. 2. (a) The population of the states $|\Psi_1^\alpha\rangle$ and $|\Psi_2^\alpha\rangle$ change with the time. The line with blue triangle ($|\Psi_1^\alpha\rangle$) and red rectangle ($|\Psi_2^\alpha\rangle$) are based on the effective Hamiltonian (15), and the dashed blue line ($|\Psi_1^\alpha\rangle$) and solid red line ($|\Psi_2^\alpha\rangle$) are based on the original Hamiltonian (6). Under the condition $\Gamma \gg \delta \gg \Omega_{13}^\alpha, \Omega_{23}^\alpha$, state $|\Psi_3^{\alpha-1}\rangle$ can be eliminated and, thus, obtain an effective transition between $|\Psi_1^\alpha\rangle$ and $|\Psi_2^\alpha\rangle$. Here, we take $N = \alpha = 2$ for an example, and $\delta = 10\,\Omega_2$, $\Gamma = 1000\,\Omega_2$. (b) The main step for generating any state $|\Psi_{1,2}^\alpha\rangle$ by a far-detuning state $|\Psi_3^{\alpha-1}\rangle$ within the DFS.

excitation,

$$\hat{H}_D = \frac{\Omega^\alpha}{2} |\Psi_2^\alpha\rangle\langle\Psi_1^\alpha| + \text{H.c.}, \quad (15)$$

where $|\Omega^\alpha| = |\Omega_d|\alpha/(N_\alpha + 1)$ and $|\Omega_d| = |\Omega_2|^2/2\delta$. We display this off-resonance two-photon transition process in Fig. 2(a). The lines with solid symbols represent the results simulated by the effective Hamiltonian (15). It presents a perfect Rabi oscillation between the states $|\Psi_1^2\rangle$ (blue triangle) and $|\Psi_2^2\rangle$ (red rectangle). In addition, we also plot the evolution of those two states based on the original Hamiltonian (6), denoted by the dashed blue line for $|\Psi_1^2\rangle$ and the solid red line for $|\Psi_2^2\rangle$. Different from the ideal case, we can find a tiny decay of the Rabi oscillation because a few population leaks out of the DFS. So far, we can flip state $|\Psi_1^\alpha\rangle \rightarrow |\Psi_2^{\alpha+1}\rangle$ of the ancilla center by applying the control field Ω_1 and then flip $|\Psi_2^{\alpha+1}\rangle \rightarrow |\Psi_1^{\alpha+1}\rangle$ with $\Omega^{\alpha+1}$ at the same time re-initialize the process [77]. Therefore, we can generate any $|\Psi_{1,2}^\alpha\rangle$ by using a combination of α off-resonance Raman transitions and α control fields. In Fig. 2(b), we sketch the protocol steps for this process.

IV. PREPARATION OF GHZ STATES

We follow the approach given in Ref. [79] to produce the effective Rabi-frequency sequences. We assume that the initial state is $|F_0\rangle = |\Psi_1^0\rangle$, i.e., all the SiV centers are in state $|1\rangle$. After a target time t^*, the system evolves into a GHZ state

with the form

$$|\text{GHZ}\rangle_N = \frac{1}{\sqrt{2}}(|\overbrace{1\cdots 1}^{N}\rangle + |\overbrace{2\cdots 2}^{N}\rangle) \otimes |1\rangle_A$$

$$\equiv \frac{1}{\sqrt{2}}\big(|\Psi_1^0\rangle + |\Psi_1^N\rangle\big). \tag{16}$$

We first divide the time interval into $2N$ subintervals, and all subintervals have equal lengths $\tau = t^*/2N$. From the previous section, one can find that Ω^α and Ω_1 are applied alternately. We, thus, prescribe that for $2(l-1)\tau < t < (2l-1)\tau$, $\Omega_1(t) = \Omega_{1l}$, $\Omega^\alpha(t) = 0$, and for $(2l-1)\tau < t < 2l\tau$, $\Omega_1(t) = 0$, $\Omega^\alpha(t) = \Omega_l^\alpha$, where $1 \leqslant l \leqslant N$. The time-evolution operator of the SiV centers can be expressed as

$$U(t^*) = D_N C_N D_{N-1} C_{N-1} \cdots D_2 C_2 D_1 C_1, \tag{17}$$

where C_l and D_l describes the evolution due to the control field $\hat{H}_{12}^C$ and the effective Hamiltonian $\hat{H}_D$, respectively. These two operators can be expressed in the form of a 2×2 matrix in the basis of $\{|\Psi_1^{\alpha-1}\rangle, |\Psi_2^\alpha\rangle\}$ and $\{|\Psi_2^\alpha\rangle, |\Psi_1^\alpha\rangle\}$,

$$C_l = \begin{bmatrix} \cos\frac{|\Omega_{1l}|\tau}{2} & -ie^{i\theta_l}\sin\frac{|\Omega_{1l}|\tau}{2} \\ -ie^{-i\theta_l}\sin\frac{|\Omega_{1l}|\tau}{2} & \cos\frac{|\Omega_{1l}|\tau}{2} \end{bmatrix},$$

$$D_l = \begin{bmatrix} \cos\frac{|\Omega_l^\alpha|\tau}{2} & -ie^{i\phi_l}\sin\frac{|\Omega_l^\alpha|\tau}{2} \\ -ie^{-i\phi_l}\sin\frac{|\Omega_l^\alpha|\tau}{2} & \cos\frac{|\Omega_l^\alpha|\tau}{2} \end{bmatrix}. \tag{18}$$

Here, $\Omega_{1l} = |\Omega_{1l}|e^{i\theta_l}$ and $\Omega_l^\alpha = |\Omega_l^\alpha|e^{i\phi_l}$. In order to determine the values for $\{\Omega_{1l}\}$ and $\{\Omega_l^\alpha\}$, we can calculate the inverse evolution from the target state $|F_N\rangle$, that is $|F_0\rangle = C_1^\dagger D_1^\dagger \cdots C_{N-1}^\dagger D_{N-1}^\dagger C_N^\dagger D_N^\dagger |F_N\rangle$. We assume that state $|F_{l-1}\rangle = C_l^\dagger D_l^\dagger C_{l+1}^\dagger D_{l+1}^\dagger \cdots C_N^\dagger D_N^\dagger |F_N\rangle$ is a middle state. When $C_l^\dagger D_l^\dagger$ acts on $|F_l\rangle$, all populations in $|\Psi_1^l\rangle$ and $|\Psi_2^l\rangle$ are transferred to $|\Psi_1^{l-1}\rangle$ and $|\Psi_2^{l-1}\rangle$. Repeating this process, state $|F_N\rangle$ can be brought to $|F_0\rangle$ eventually. Thus, we can obtain the following equations for each state $|F_l\rangle$:

$$\langle\Psi_1^l|D_l^\dagger|F_l\rangle = 0,$$

$$\langle\Psi_2^l|C_l^\dagger D_l^\dagger|F_l\rangle = 0. \tag{19}$$

Here, these two equations are complex number equations and can be rewritten as four real number equations corresponding to each l from which we can numerically solve the four parameters $|\Omega_{1l}|$, θ_l, $|\Omega_l^\alpha|$, and ϕ_l. Note that the solutions of the four parameters are not unique, and we can obtain the pulse sequence by running l from N to 0.

Next, we take $N = 4$ as an example. In Table I, we show the pulse sequences for generating the specific GHZ state of $N = 4$, i.e., $|\text{GHZ}\rangle_4 = \frac{1}{\sqrt{2}}(|1111\rangle + |2222\rangle) \otimes |1\rangle_A$ and plot the evolution process in Fig. 3. We apply the Hamiltonian $\hat{H}_{12}^C$ in the white background and Hamiltonian $\hat{H}_D$ in the gray background of Fig. 3(a). We stop the pulse at the vertical dashed black line. For generating $|\text{GHZ}\rangle_N$, we need to apply $2N$ operations. We find that the fidelity (the line with the red rhomboid) reaches one, which means entangled state $|\text{GHZ}\rangle_4$ can be perfectly generated. A more precise process of the states evolution is shown in Fig. 3(b). The initial state is $|\Psi_1^0\rangle$. Under each pulse, the Hilbert space is always divided into several independent two-dimensional subspaces, and the transition occurs only within each subspace. On the one hand,

TABLE I. $N = 4$. The pulse sequences of $\{\Omega_{1l}\tau\}$ and $\{\Omega_{dl}\tau\}$ for the generation of state $|\text{GHZ}\rangle_4 = \frac{1}{\sqrt{2}}(|1111\rangle + |2222\rangle) \otimes |1\rangle_A$. Here, $|\Omega_l^\alpha| = |\Omega_{dl}|\alpha/(N_\alpha + 1)$. And we apply the pulse from the top of the table to bottom in sequence.

	l	$|\Omega_{1l}\tau|$	$\arg(\Omega_{1l}\tau)$	$|\Omega_{dl}\tau|$	$\arg(\Omega_{dl}\tau)$
C_1	1	π	π		
D_1	1			8.33	π
C_2	2	π	π		
D_2	2			7.48	π
C_3	3	π	π		
D_3	3			3.14	π
C_4	4	π	π		
D_4	4			1.57	π

each H_{12}^C causes a complete transition between the two states in the Hilbert subspace. On the other hand, the first pulse of H_D transfers part of probabilities (more than half) from $|\Psi_2^1\rangle$ to $|\Psi_1^1\rangle$, whereas the other part remains in state $|\Psi_2^1\rangle$. During the second pulse of H_D, the probability of state $|\Psi_1^0\rangle$ remain unchanged as it does not participate in the transition under H_D, and the probability of state $|\Psi_2^2\rangle$ becomes 0.5. The residual probability will be integrated into state $|\Psi_2^1\rangle$ in the third pulse of H_D. Now, states $|\Psi_2^1\rangle$ and $|\Psi_1^3\rangle$ have the same population. Subsequently, the system evolves into target state $|\text{GHZ}\rangle_4$.
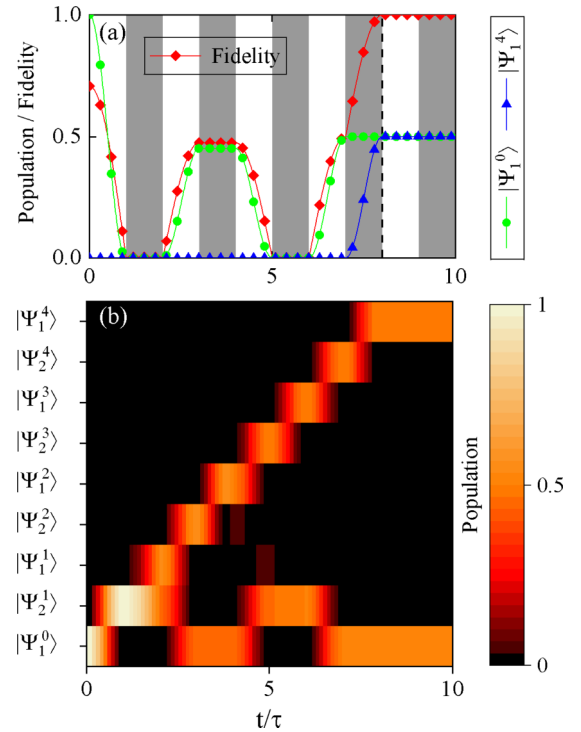

FIG. 3. The generation of $|\text{GHZ}\rangle_4 = \frac{1}{\sqrt{2}}(|1111\rangle + |2222\rangle) \otimes |1\rangle_A$. (a) Time evolution of the fidelity (the line with the red rhomboid) of $|\text{GHZ}\rangle_4$ and the populations of state $|\Psi_1^0\rangle$ (the line with the green circle), and$|\Psi_1^4\rangle$ (the line with the blue triangle). The white and gray background corresponds to the Hamiltonian $\hat{H}_{12}^C$ and $\hat{H}_D$, respectively. The vertical dashed black line indicates that the pulse is stopped. (b) Evolution of the corresponding probability distribution.
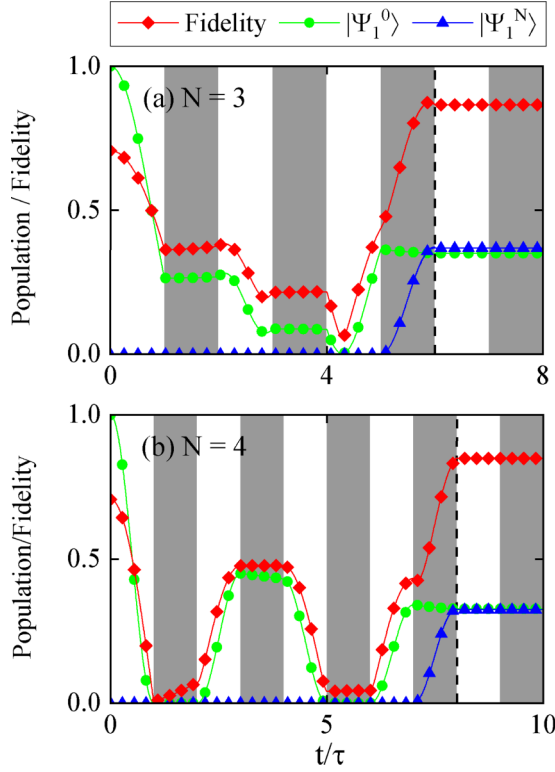
FIG. 4. The fidelity under the original Hamiltonian (6) for (a) $N = 3$ and (b) $N = 4$. Here, we choose $\delta = 50 \max\{\Omega_d\}$ and $\Gamma = 20\delta$. The fidelity of $N = 3$ and $N = 4$ can reach 0.866 and 0.849, respectively.

So far, we have analyzed the ideal situation. Next, in order to estimate the realistic fidelities with the finite collective decay rate Γ, we need to take the errors into consideration. We can consider this error intuitively via the original Hamiltonian (6) where we do not make any approximations. And the master equation is described by

$$\dot{\rho} = -i[\hat{H}, \hat{\rho}] + \Gamma D[\hat{S}_-]\hat{\rho}, \tag{20}$$

where $\hat{H} = \hat{H}_{12}^C + \hat{H}_{23}^D$ is from the original Hamiltonian (6). We plot the fidelity and population for the preparation of states $|GHZ\rangle_3$ and $|GHZ\rangle_4$ in Fig. 4. Here, the line with the red rhomboid, green cycle, and blue triangle still denotes the fidelity and the population of $|\Psi_1^0\rangle$, $|\Psi_1^N\rangle$. In this case, the fidelity of states $|GHZ\rangle_3$ and $|GHZ\rangle_4$ can reach up to 0.866 and 0.849, respectively, and it decreases with the increase in the particle number. In addition, Fig. 4(b) has the same parameters as Fig. 3(a) for $N = 4$ except for the collective decay rate. Although the finite collective dissipation rate leads to a decrease in the fidelity, the final state is in the decoherence free subspace and is not affected by dissipation.

V. ERROR AND DISORDER

In this section, we consider the effect of collective decay rate, imperfect position, and the inhomogeneous strain coupling on fidelity. In Figs. 5(a) and 5(b), we analyze the effect of different collective decay rates $\Gamma = 20\delta$ and $\Gamma = 200\delta$ within the two-photon transition process for $N = 2$, and $\alpha = 2$. Actually, we separate the whole Hilbert space into
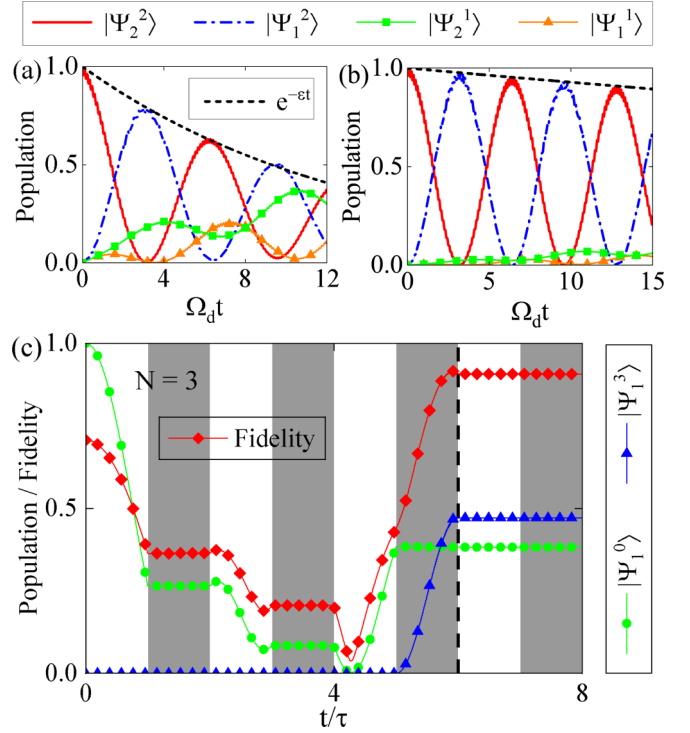

FIG. 5. Error analysis within the two-photon transition for different decay rates: (a) $\Gamma = 20\delta$, (b) $\Gamma = 200\delta$ with $N = \alpha = 2$. (c) Time evolution of the fidelity (the line with the red rhomboid) of $|GHZ\rangle_3$ and the populations of state $|\Psi_1^0\rangle$ (the line with the green circle), $|\Psi_1^3\rangle$ (the line with the blue triangle) for $\Gamma = 200\delta$.

two subspaces by projecting: DFS states ($|\Psi_1^\alpha\rangle$, $|\Psi_2^\alpha\rangle$, $|\Psi_3^\alpha\rangle$) ($\alpha = 0$–2) and non-DFS states (e.g., $|\chi_1^{\alpha-1}\rangle$, $|\chi_2^{\alpha-1}\rangle$). The Hamiltonian H_{23}^D drives the damped oscillation of the population between states $|\Psi_1^2\rangle$ (dot-dashed blue line) and $|\Psi_2^2\rangle$ (solid red line). A small part of the population leaks into states $|\chi_1^1\rangle$ and $|\chi_2^1\rangle$ and then decays to $|\Psi_1^1\rangle$ (the line with the orange triangle) and $|\Psi_2^1\rangle$ (the line with the green rectangle) due to the enhanced decay rate $\Gamma_e = (N_\alpha + 1)\Gamma$. In addition, the Hamiltonian H_{23}^D will drive the transition between $|\Psi_1^1\rangle$ and $|\Psi_2^1\rangle$ at the same time, resulting in a slight oscillation between them. As $|\Psi_1^1\rangle$ and $|\Psi_2^1\rangle$ are inside the DFS, their total populations will accumulate over time constantly. The loss for the off-resonance two-photon transition process of each α is given by two parts [77],

$$\epsilon_1^\alpha = \Gamma_e \frac{\alpha N_\alpha |\Omega_2|^2}{4(N_\alpha + 1)(\delta^2 + \Gamma_e^2)} + \Gamma_e \frac{\alpha |\Omega_2|^2}{4N_\alpha(N_\alpha + 1)(\delta^2 + \Gamma_e^2)},$$

$$\epsilon_2^\alpha = \Gamma_e \frac{(\alpha - 1)|\Omega_2|^2}{4(\delta^2 + \Gamma_e^2)}. \tag{21}$$

The damping $e^{-\epsilon^\alpha t}$ (dotted black line) with the rate $\epsilon^\alpha = \epsilon_1^\alpha + \epsilon_2^\alpha$ perfectly fits the dynamic envelope as shown in Figs. 5(a) and 5(b). In addition, we can find that the error ϵ^α for the fixed α will be slightly reduced with increasing the number of the center in the case of $\Gamma \gg \delta$. Note that in optical waveguides, emitters have an irreversible lost to free space, which can be characterized by the Purcell factor, the ratio of the emission rate into the waveguide modes and the

one into nonguided modes [80]. For a too small Purcell factor, each quantum emitter would have a non-negligible free-space emission, leading to a faster decay of the DFS. This is not the case for the phonon waveguide in this scheme as phonons cannot exist in free space [75,81]. And, thus, we here do not need to consider the error from the emitter radiating into the vacuum.

By comparing Figs. 5(a) and 5(b), we show the effect of different collective decay rate Γ on the error. We find that the error significantly decreases with the enhancement of the collective decay rate Γ. We can explain this conclusion from the perspective of the quantum Zeno effect, which suggests that frequent measurements of the initial state hinder its dynamics to evolve to other states [82–84]. The 1D waveguide and the SiV centers behave as a system under observation where the time between two consecutive measurements is proportional to $\sim 1/\Gamma_e$. We are interested in the regime of strong collective dissipation, i.e., $\Gamma_e \gg \Omega_1,\ \Omega_2,\ \Omega_2',\ \delta$ [77]. It means the time between two consecutive measurements is short enough, and the 1D waveguide, thus, can be considered as a bath and continuously monitor the atomic state just as in the quantum Zeno regime [77,85,86]. In this case, any process that would lead the state out of the DFS is forbidden by the measurement and always projects the system back into a DFS state [87]. Besides, we find that the loss rate $\epsilon^\alpha \propto 1/\Gamma_e$, which shows that the infinite collective decay rate guarantees lossless decoherence free subspaces. And we can improve the fidelity by increasing the collective decay rate Γ. In addition, we plot the fidelity in the case of the enhanced collective decay rate $\Gamma = 200\delta$ for $N = 3$ in Fig. 5(c). When the collective decay rate increases by tenfold, the fidelity is improved to 0.907, and this only requires a threefold increase in the coupling strength of the SiV center to the waveguide.

For experimental realizations, we study the effect of two types of disorder: One appears in the position of SiV centers, and the other appears in the strain coupling. First, we consider the imperfect position x_n of the nth SiV center with a disorder $w\chi_i$, where χ_i is a random number uniformly distribution in $[-1, 1]$ and w is the disorder strength. We plot in Figs. 6(a) and 6(b) the evolution for the situation $w = 0.03\pi/k(\Delta)$ and $w = 0.06\pi/k(\Delta)$. When w is very small, there is almost no observable effect. With the increase in w, the population of states $|\Psi_1^{0/2}\rangle$ is almost constant, but the fidelity has a obvious decay. Actually, due to the collective decay rate $G_{nm} \propto e^{ik(\Delta)(x_n-x_m)}$, the imperfect position mainly affects the phase of the final state. We, thus, can assume the final state is $|F_N\rangle = \frac{1}{\sqrt{2}}(|\Psi_1^0\rangle + e^{i\theta}|\Psi_1^N\rangle)$ [88], where θ is a small relative phase and depends on the disorder. Therefore, the population of states $|\Psi_1^{0/N}\rangle$ remain unchanged, whereas the fidelity reduces to $1 - \theta^2/8$. We only present the results for $N = 2$ as it takes too long a time to simulate a large system, but it is obvious that disorder will accumulate with the increase in center number, which results in a more significant decay of fidelity.

Next, we analyze the effect of inhomogeneous coupling. This effect is reflected mainly on the amplitude of the final state because of the collective decay rate $G_{nm} \propto g_{j,k}^n g_{j,k}^m$. We consider a small error η in the amplitude, i.e., $|F_N\rangle = \frac{1}{\sqrt{2}}(\sqrt{1+\eta}|\Psi_1^0\rangle + \sqrt{1-\eta}|\Psi_1^N\rangle)$. The population becomes
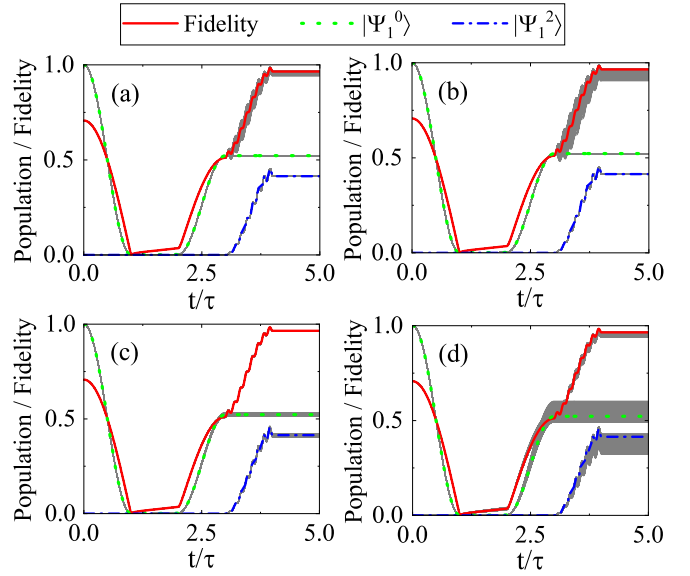

FIG. 6. Evolution of the fidelity (solid red line), population of $|\Psi_1^0\rangle$ (dashed green line), and $|\Psi_1^2\rangle$ (dot-dashed blue line) without and with disorder with the standard deviations marked in gray shadows when (a) $w = 0.03\pi/k(\Delta)$, (b) $w = 0.06\pi/k(\Delta)$ for the imperfect position, (c) $w = 0.025g$, and (d) $w = 0.15g$ for inhomogeneous coupling with 400 random configurations. Here, $N = 2$, $\delta = 10 \max\{\Omega_d\}$, and $\Gamma = 100\delta$.

$(1 \pm \eta)/2$, whereas the fidelity has a second-order error $\eta^2/8$. Therefore, there is a significant broadening on populations but a slight decay on fidelity in Figs. 6(c) and 6(d) even with a disorder $w = 0.15g$.

In order to intuitively discuss the impact of position imperfection and inhomogeneous coupling, we also plot the fidelity in different disorder strength w for $N = 2$ in Fig. 7 with
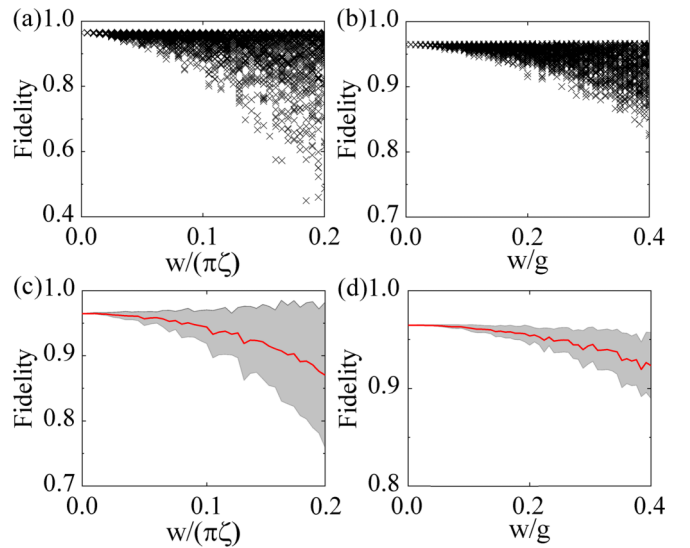

FIG. 7. Fidelity with different disorder strength w for (a) and (c) position imperfections and (b) and (d) inhomogeneous couplings with 100 random configurations. In (c) and (d), the solid red line is the mean value by averaging over 100 random configurations, and the standard deviations are marked in gray. Here, $N = 2$, $\zeta = 1/k(\Delta)$, $\delta = 10 \max\{\Omega_d\}$, and $\Gamma = 100\delta$.

100 random configurations. In Figs. 7(a) and 7(b), each cross corresponds to the fidelity of the final steady state. We can conclude that the disorder would have an increasing impact for larger systems with the increase in w. In Figs. 7(c) and 7(d), the solid red line presents the mean value of the fidelity, and the standard deviations are marked in gray shadows. This shows that the system is sensitive to positional imperfections but more tolerant to inhomogeneous coupling.

VI. EXPERIMENTAL FEASIBILITY

This hybrid spin-phononic system consists of an array of $N + 1$ SiV centers embedded in a 1D waveguide, and the auxiliary center needs to be addressed individually. With the development of state-of-the-art nanofabrication techniques, it has been demonstrated that SiV center arrays can be efficiently generated through ion implementation techniques [89,90]. This means that the proposed setup can be achieved experimentally. For the acoustic diamond waveguide, the length and cross section are $L = 100\ \mu\mathrm{m}$ and $A = 80 \times 80\ \mathrm{nm}^2$ [75]. In addition, the material properties of the diamond waveguide are $\rho = 3500\ \mathrm{kg/m^3}$, $E = 1050\ \mathrm{GPa}$, and $\nu = 0.2$. The SiV center mainly couples to the longitudinal compression mode with the group velocity $v \sim 10^4\ \mathrm{m/s}$ [75]. Under these conditions, we can calculate the strain coupling strength $g/2\pi \approx 8.2$ MHz and phonon-induced decay rate $\Gamma/2\pi \approx 8.5$ MHz.

We then take $N = 3$ and $N = 4$ as examples to simulate the fidelity of the GHZ state. In the quantum Zeno regime, we have $\Gamma_e \gg \Omega_1,\ \Omega_2,\ \Omega_2',\ \delta$ [77]. Therefore, we assume the detuning $\delta = \Gamma/20 \approx 2\pi \times 0.4$ MHz, and $\max\{\Omega_d\} = \delta/50 = 2\pi \times 8.5$ kHz, which corresponds to the maximum dimensionless pulse sequences 8.33 of Table I for $N = 4$. We can derive the realistic total time $t^* = 2N\tau = 1.2$ ms for generating $|\mathrm{GHZ}\rangle_4 = \frac{1}{\sqrt{2}}(|1111\rangle + |2222\rangle) \otimes |1\rangle_A$, which is shorter than the spin coherence time.

In this scheme, we need to precisely choose the positions of the SiV centers such that $x_n = n\lambda_0 = 2n\pi/k(\Delta)$ ($n \in \mathbb{N}$). However, such a condition cannot be perfectly realized experimentally, and we have discussed the effect of imperfect positions in Sec. V. It shows that this scheme can tolerate the error of 6%, at least, which means a 12-nm uncertainty of the position of the SiV centers. In addition, the precise positioning

of SiV centers with tens of nanometers accuracy was reported in Ref. [89]. Moreover, the fidelity is almost unaffected for inhomogeneous strain coupling even with the error of 15%.

VII. CONCLUSION

In conclusion, we have proposed a scheme to generate GHZ states based on a solid-state setup where an array of $N + 1$ SiV centers are embedded in a 1D diamond waveguide. We here apply two driving fields H_{12}^C and H_{23}^D, which control the ancilla center and the first N SiV centers. By projecting the spin states into DFS, the whole Hilbert space is divided into two parts: the states inside the DFS and the states outside the DFS. The states inside the DFS can avoid the collective dissipation. We next achieve a ladderlike coupling structure in DFS by alternating between a two-photon Raman transition and the control fields on the ancilla. Here, we need to apply $2N$ operations to generate $|\mathrm{GHZ}\rangle_N$, and the final state is within the DFS. Compared with some dynamical methods for preparing GHZ states [34,91], this scheme generates a steady-state entangled state. This is because the target state $|\mathrm{GHZ}\rangle_N$ is prepared in DFS, which is immune to decoherence.

We also analyze the errors that may occur within each step α. As phonons cannot spread in the vacuum, we only need to consider the errors due to the phonons emitted from the states out of the DFS. In this scheme, the fidelity is sensitive to the collective decay rate Γ. We can improve the fidelity by enhancing the coupling strength between the SiV centers and the waveguide. In addition, using ion implementation techniques to accurately locate the color centers can also reduce the effect of position imperfections on the fidelity. Moreover, we analyze the effects due to the position imperfection of SiV centers and the inhomogeneous coupling between the center and waveguide modes. This paper may provide a realistic and feasible platform for generating the GHZ state in a solid-state system.

[1] S.-B. Zheng and G.-C. Guo, Efficient Scheme for Two-Atom Entanglement and Quantum Information Processing in Cavity QED, Phys. Rev. Lett. **85**, 2392 (2000).

[2] R. Horodecki, P. Horodecki, M. Horodecki, and K. Horodecki, Quantum entanglement, Rev. Mod. Phys. **81**, 865 (2009).

[3] N. Friis, G. Vitagliano, M. Malik, and M. Huber, Entanglement certification from theory to experiment, Nat. Rev. Phys. **1**, 72 (2019).

[4] H. Krauter, C. A. Muschik, K. Jensen, W. Wasilewski, J. M. Petersen, J. I. Cirac, and E. S. Polzik, Entanglement Generated by Dissipation and Steady State Entanglement of Two Macroscopic Objects, Phys. Rev. Lett. **107**, 080503 (2011).

[5] C. H. Bennett, G. Brassard, C. Crépeau, R. Jozsa, A. Peres, and W. K. Wootters, Teleporting an Unknown Quantum State Via Dual Classical and Einstein-Podolsky-Rosen Channels, Phys. Rev. Lett. **70**, 1895 (1993).

[6] N. Gisin, G. Ribordy, W. Tittel, and H. Zbinden, Quantum cryptography, Rev. Mod. Phys. **74**, 145 (2002).

[7] A. K. Ekert, Quantum Cryptography Based on Bell's Theorem, Phys. Rev. Lett. **67**, 661 (1991).

[8] C. Schimpf, M. Reindl, D. Huber, B. Lehner, S. F. C. D. Silva, S. Manna, M. Vyvlecka, P. Walther, and A. Rastelli, Quantum cryptography with highly entangled photons from semiconductor quantum dots, Sci. Adv. **7**, eabe8905 (2021).

[9] N. Lambert, C. Emary, and T. Brandes, Entanglement and the Phase Transition in Single-Mode Superradiance, Phys. Rev. Lett. **92**, 073602 (2004).

[10] H. Yu and W. Yao, Entanglement detection and quantum metrology by Raman photon-diffraction imaging, Phys. Rev. A **87**, 042303 (2013).

[11] V. Vedral, High-temperature macroscopic entanglement, New J. Phys. **6**, 102 (2004).

[12] J.-Q. Chen, Y.-F. Qiao, X.-L. Dong, X.-L. Hei, and P.-B. Li, Dissipation-assisted preparation of steady spin-squeezed states of SiV centers, Phys. Rev. A **103**, 013709 (2021).

[13] A. Barasiński, A. Černoch, K. Lemr, and J. Soubusta, Genuine tripartite nonlocality for random measurements in Greenberger-Horne-Zeilinger-class states and its experimental test, Phys. Rev. A **101**, 052109 (2020).

[14] V. Caprara Vivoli, J. Ribeiro, and S. Wehner, High-fidelity Greenberger-Horne-Zeilinger state generation within nearby nodes, Phys. Rev. A **100**, 032310 (2019).

[15] K. Xia and J. Twamley, Generating spin squeezing states and Greenberger-Horne-Zeilinger entanglement using a hybrid phonon-spin ensemble in diamond, Phys. Rev. B **94**, 205118 (2016).

[16] C. Eltschka and J. Siewert, Entanglement of Three-Qubit Greenberger-Horne-Zeilinger–Symmetric States, Phys. Rev. Lett. **108**, 020502 (2012).

[17] J. Chen, H. Zhou, C. Duan, and X. Peng, Preparing Greenberger-Horne-Zeilinger and *W* states on a long-range Ising spin model by global controls, Phys. Rev. A **95**, 032340 (2017).

[18] Y.-F. Qiao, H.-Z. Li, X.-L. Dong, J.-Q. Chen, Y. Zhou, and P.-B. Li, Phononic-waveguide-assisted steady-state entanglement of silicon-vacancy centers, Phys. Rev. A **101**, 042313 (2020).

[19] X. Q. Shao, J. H. Wu, X. X. Yi, and G.-L. Long, Dissipative preparation of steady Greenberger-Horne-Zeilinger states for Rydberg atoms with quantum Zeno dynamics, Phys. Rev. A **96**, 062315 (2017).

[20] M. Płodzień, M. Kościelski, E. Witkowska, and A. Sinatra, Producing and storing spin-squeezed states and Greenberger-Horne-Zeilinger states in a one-dimensional optical lattice, Phys. Rev. A **102**, 013328 (2020).

[21] S.-L. Su, X.-Q. Shao, H.-F. Wang, and S. Zhang, Scheme for entanglement generation in an atom-cavity system via dissipation, Phys. Rev. A **90**, 054302 (2014).

[22] Z. Jin, S. L. Su, and S. Zhang, Preparation of a steady entangled state of two nitrogen-vacancy centers by simultaneously utilizing two dissipative factors, Phys. Rev. A **100**, 052332 (2019).

[23] Y. Zhang, T. Liu, J. Zhao, Y. Yu, and C.-P. Yang, Generation of hybrid Greenberger-Horne-Zeilinger entangled states of particlelike and wavelike optical qubits in circuit QED, Phys. Rev. A **101**, 062334 (2020).

[24] D. M. Greenberger, M. A. Horne, A. Shimony, and A. Zeilinger, Bell's theorem without inequalities, Am. J. Phys. **58**, 1131 (1990).

[25] R.-H. Zheng, Y.-H. Kang, D. Ran, Z.-C. Shi, and Y. Xia, Deterministic interconversions between the Greenberger-Horne-Zeilinger states and the *W* states by invariant-based pulse design, Phys. Rev. A **101**, 012345 (2020).

[26] D. Bouwmeester, J.-W. Pan, M. Daniell, H. Weinfurter, and A. Zeilinger, Observation of Three-Photon Greenberger-Horne-Zeilinger Entanglement, Phys. Rev. Lett. **82**, 1345 (1999).

[27] K. X. Wei, I. Lauer, S. Srinivasan, N. Sundaresan, D. T. McClure, D. Toyli, D. C. McKay, J. M. Gambetta, and S. Sheldon, Verifying multipartite entangled Greenberger-Horne-Zeilinger states via multiple quantum coherences, Phys. Rev. A **101**, 032343 (2020).

[28] J.-X. Han, J.-L. Wu, Y. Wang, Y. Xia, Y.-Y. Jiang, and J. Song, Large-scale Greenberger-Horne-Zeilinger states through a topologically protected zero-energy mode in a superconducting qutrit-resonator chain, Phys. Rev. A **103**, 032402 (2021).

[29] Q. Zhao, G. Wang, X. Yuan, and X. Ma, Efficient and robust detection of multipartite Greenberger-Horne-Zeilinger-like states, Phys. Rev. A **99**, 052349 (2019).

[30] K. F. Pál, T. Vértesi, and N. Brunner, Closing the detection loophole in multipartite Bell tests using Greenberger-Horne-Zeilinger states, Phys. Rev. A **86**, 062111 (2012).

[31] Y. Zhou, B. Li, X.-X. Li, F.-L. Li, and P.-B. Li, Preparing multiparticle entangled states of nitrogen-vacancy centers via adiabatic ground-state transitions, Phys. Rev. A **98**, 052346 (2018).

[32] T. Li, A. Miranowicz, K. Xia, and F. Nori, Resource-efficient analyzer of Bell and Greenberger-Horne-Zeilinger states of multiphoton systems, Phys. Rev. A **100**, 052302 (2019).

[33] U. Sakaguchi, H. Ozawa, C. Amano, and T. Fukumi, Microscopic analogs of the Greenberger-Horne-Zeilinger experiment on an NMR quantum computer, Phys. Rev. A **60**, 1906 (1999).

[34] C. Song, K. Xu, H. Li, Y.-R. Zhang, X. Zhang, W. Liu, Q. Guo, Z. Wang, W. Ren, J. Hao *et al.*, Generation of multicomponent atomic Schrödinger cat states of up to 20 qubits, Science **365**, 574 (2019).

[35] X.-L. Wang, Y.-H. Luo, H.-L. Huang, M.-C. Chen, Z.-E. Su, C. Liu, C. Chen, W. Li, Y.-Q. Fang, X. Jiang, J. Zhang, L. Li, N.-L. Liu, C.-Y. Lu, and J.-W. Pan, 18-Qubit Entanglement with Six Photons' Three Degrees of Freedom, Phys. Rev. Lett. **120**, 260502 (2018).

[36] A. Omran, H. Levine, A. Keesling, G. Semeghini, T. T. Wang, S. Ebadi, H. Bernien, A. S. Zibrov, H. Pichler, S. Choi *et al.*, Generation and manipulation of Schrödinger cat states in Rydberg atom arrays, Science **365**, 570 (2019).

[37] R. Mukherjee, H. Xie, and F. Mintert, Bayesian Optimal Control of Greenberger-Horne-Zeilinger States in Rydberg Lattices, Phys. Rev. Lett. **125**, 203603 (2020).

[38] Y. Ji, J. Bian, X. Chen, J. Li, X. Nie, H. Zhou, and X. Peng, Experimental preparation of Greenberger-Horne-Zeilinger states in an Ising spin model by partially suppressing the nonadiabatic transitions, Phys. Rev. A **99**, 032323 (2019).

[39] T. P. Gujarati, Rydberg-atom-based creation of an *n*-particle Greenberger-Horne-Zeilinger state using stimulated Raman adiabatic passage, Phys. Rev. A **98**, 062326 (2018).

[40] B. Alexander, J. J. Bollinger, and H. Uys, Generating Greenberger-Horne-Zeilinger states with squeezing and postselection, Phys. Rev. A **101**, 062303 (2020).

[41] C. Hepp, T. Müller, V. Waselowski, J. N. Becker, B. Pingault, H. Sternschulte, D. Steinmüller-Nethl, A. Gali, J. R. Maze, M. Atatüre, and C. Becher, Electronic Structure of the Silicon Vacancy Color Center in Diamond, Phys. Rev. Lett. **112**, 036405 (2014).

[42] B. Pingault, J. N. Becker, C. H. H. Schulte, C. Arend, C. Hepp, T. Godde, A. I. Tartakovskii, M. Markham, C. Becher, and M. Atatüre, All-Optical Formation of Coherent Dark States

of Silicon-Vacancy Spins in Diamond, Phys. Rev. Lett. **113**, 263601 (2014).

[43] X.-X. Li, B. Li, and P.-B. Li, Simulation of topological phases with color center arrays in phononic crystals, Phys. Rev. Research **2**, 013121 (2020).

[44] L. J. Rogers, K. D. Jahnke, M. H. Metsch, A. Sipahigil, J. M. Binder, T. Teraji, H. Sumiya, J. Isoya, M. D. Lukin, P. Hemmer, and F. Jelezko, All-optical Initialization, Readout, and Coherent Preparation of Single Silicon-Vacancy Spins in Diamond, Phys. Rev. Lett. **113**, 263602 (2014).

[45] C. Weinzetl, J. Görlitz, J. N. Becker, I. A. Walmsley, E. Poem, J. Nunn, and C. Becher, Coherent Control and Wave Mixing in An Ensemble of Silicon-Vacancy Centers in Diamond, Phys. Rev. Lett. **122**, 063601 (2019).

[46] L. J. Rogers, K. D. Jahnke, M. W. Doherty, A. Dietrich, L. P. McGuinness, C. Müller, T. Teraji, H. Sumiya, J. Isoya, N. B. Manson, and F. Jelezko, Electronic structure of the negatively charged silicon-vacancy center in diamond, Phys. Rev. B **89**, 235101 (2014).

[47] J. M. Higbie, J. D. Perreault, V. M. Acosta, C. Belthangady, P. Lebel, M. H. Kim, K. Nguyen, V. Demas, V. Bajaj, and C. Santori, Multiphoton-Excited Fluorescence of Silicon-Vacancy Color Centers in Diamond, Phys. Rev. Appl. **7**, 054010 (2017).

[48] M. H. Metsch, K. Senkalla, B. Tratzmiller, J. Scheuer, M. Kern, J. Achard, A. Tallaire, M. B. Plenio, P. Siyushev, and F. Jelezko, Initialization and Readout of Nuclear Spins Via a Negatively Charged Silicon-vacancy Center in Diamond, Phys. Rev. Lett. **122**, 190503 (2019).

[49] X.-L. Dong, P.-B. Li, T. Liu, and F. Nori, Unconventional Quantum Sound-Matter Interactions in Spin-Optomechanical-Crystal Hybrid Systems, Phys. Rev. Lett. **126**, 203601 (2021).

[50] X.-X. Li, P.-B. Li, H.-R. Li, H. Gao, and F.-L. Li, Simulation of topological Zak phase in spin-phononic crystal networks, Phys. Rev. Research **3**, 013025 (2021).

[51] A. Sipahigil, K. D. Jahnke, L. J. Rogers, T. Teraji, J. Isoya, A. S. Zibrov, F. Jelezko, and M. D. Lukin, Indistinguishable Photons From Separated Silicon-Vacancy Centers in Diamond, Phys. Rev. Lett. **113**, 113602 (2014).

[52] C. Arend, J. N. Becker, H. Sternschulte, D. Steinmüller-Nethl, and C. Becher, Photoluminescence excitation and spectral hole burning spectroscopy of silicon vacancy centers in diamond, Phys. Rev. B **94**, 045203 (2016).

[53] S. Meesala, Y.-I. Sohn, B. Pingault, L. Shao, H. A. Atikian, J. Holzgrafe, M. Gündoğan, C. Stavrakas, A. Sipahigil, C. Chia, R. Evans, M. J. Burek, M. Zhang, L. Wu, J. L. Pacheco, J. Abraham, E. Bielejec, M. D. Lukin, M. Atatüre, and M. Lončar, Strain engineering of the silicon-vacancy center in diamond, Phys. Rev. B **97**, 205444 (2018).

[54] L. J. Rogers, O. Wang, Y. Liu, L. Antoniuk, C. Osterkamp, V. A. Davydov, V. N. Agafonov, A. B. Filipovski, F. Jelezko, and A. Kubanek, Single Si-V^- Centers in Low-Strain Nanodiamonds with Bulklike Spectral Properties and Nanomanipulation Capabilities, Phys. Rev. Appl. **11**, 024073 (2019).

[55] J. N. Becker, B. Pingault, D. Groß, M. Gündoğan, N. Kukharchyk, M. Markham, A. Edmonds, M. Atatüre, P. Bushev, and C. Becher, All-optical Control of the Silicon-Vacancy Spin in Diamond at Millikelvin Temperatures, Phys. Rev. Lett. **120**, 053603 (2018).

[56] B. Pingault, D.-D. Jarausch, C. Hepp, L. Klintberg, J. N. Becker, M. Markham, C. Becher, and M. Atatüre, Coherent

control of the silicon-vacancy spin in diamond, Nat. Commun. **8**, 15579 (2017).

[57] S. Häußler, J. Benedikter, K. Bray, B. Regan, A. Dietrich, J. Twamley, I. Aharonovich, D. Hunger, and A. Kubanek, Diamond photonics platform based on silicon vacancy centers in a single-crystal diamond membrane and a fiber cavity, Phys. Rev. B **99**, 165310 (2019).

[58] D. D. Sukachev, A. Sipahigil, C. T. Nguyen, M. K. Bhaskar, R. E. Evans, F. Jelezko, and M. D. Lukin, Silicon-Vacancy Spin Qubit in Diamond: A Quantum Memory Exceeding 10 ms with Single-Shot State Readout, Phys. Rev. Lett. **119**, 223602 (2017).

[59] D. A. Lidar, I. L. Chuang, and K. B. Whaley, Decoherence-Free Subspaces for Quantum Computation, Phys. Rev. Lett. **81**, 2594 (1998).

[60] D. Bacon, D. A. Lidar, and K. B. Whaley, Robustness of decoherence-free subspaces for quantum computation, Phys. Rev. A **60**, 1944 (1999).

[61] V. Paulisch, H. J. Kimble, and A. González-Tudela, Universal quantum computation in waveguide QED using decoherence free subspaces, New J. Phys. **18**, 043041 (2016).

[62] J. Kattemölle and J. van Wezel, Dynamical fidelity susceptibility of decoherence-free subspaces, Phys. Rev. A **99**, 062340 (2019).

[63] W. Qin, C. Wang, and X. Zhang, Protected quantum-state transfer in decoherence-free subspaces, Phys. Rev. A **91**, 042303 (2015).

[64] J. B. Altepeter, P. G. Hadley, S. M. Wendelken, A. J. Berglund, and P. G. Kwiat, Experimental Investigation of a Two-Qubit Decoherence-Free Subspace, Phys. Rev. Lett. **92**, 147901 (2004).

[65] D. Farfurnik, R. M. Pettit, Z. Luo, and E. Waks, Single-Shot Readout of a Solid-State Spin in a Decoherence-Free Subspace, Phys. Rev. Appl. **15**, L031002 (2021).

[66] X.-M. Xiu, Q.-Y. Li, Y.-F. Lin, H.-K. Dong, L. Dong, and Y.-J. Gao, Preparation of four-photon polarization-entangled decoherence-free states employing weak cross-Kerr nonlinearities, Phys. Rev. A **94**, 042321 (2016).

[67] C.-P. Yang, Q.-P. Su, Y. Zhang, and F. Nori, Implementing a multi-target-qubit controlled-NOT gate with logical qubits outside a decoherence-free subspace and its application in creating quantum entangled states, Phys. Rev. A **101**, 032329 (2020).

[68] R. I. Karasik, K.-P. Marzlin, B. C. Sanders, and K. B. Whaley, Multiparticle decoherence-free subspaces in extended systems, Phys. Rev. A **76**, 012331 (2007).

[69] K. Macieszczak, Y.L. Zhou, S. Hofferberth, J. P. Garrahan, W. Li, and I. Lesanovsky, Metastable decoherence-free subspaces and electromagnetically induced transparency in interacting many-body systems, Phys. Rev. A **96**, 043860 (2017).

[70] F. Wang, Y.-Y. Huang, Z.-Y. Zhang, C. Zu, P.-Y. Hou, X.-X. Yuan, W.-B. Wang, W.-G. Zhang, L. He, X.-Y. Chang, and L.-M. Duan, Room-temperature storage of quantum entanglement using decoherence-free subspace in a solid-state spin system, Phys. Rev. B **96**, 134314 (2017).

[71] H. Kumagai, T. Yamamoto, M. Koashi, and N. Imoto, Robustness of quantum communication based on a decoherence-free subspace using a counter-propagating weak coherent light pulse, Phys. Rev. A **87**, 052325 (2013).

[72] K. V. Kepesidis, M.-A. Lemonde, A. Norambuena, J. R. Maze, and P. Rabl, Cooling phonons with phonons: Acoustic

reservoir engineering with silicon-vacancy centers in diamond, Phys. Rev. B **94**, 214115 (2016).

[73] A. González-Tudela and D. Porras, Mesoscopic Entanglement Induced by Spontaneous Emission in Solid-state Quantum Optics, Phys. Rev. Lett. **110**, 080502 (2013).

[74] W. Song, W. Yang, J. An, and M. Feng, Dissipation-assisted spin squeezing of nitrogen-vacancy centers coupled to a rectangular hollow metallic waveguide, Opt. Express **25**, 19226 (2017).

[75] M.-A. Lemonde, S. Meesala, A. Sipahigil, M. J. A. Schuetz, M. D. Lukin, M. Loncar, and P. Rabl, Phonon Networks with Silicon-Vacancy Centers in Diamond Waveguides, Phys. Rev. Lett. **120**, 213603 (2018).

[76] P.-B. Li, Y. Zhou, W.-B. Gao, and F. Nori, Enhancing Spin-Phonon and Spin-spin Interactions Using Linear Resources in a Hybrid Quantum System, Phys. Rev. Lett. **125**, 153602 (2020).

[77] A. González-Tudela, V. Paulisch, D. E. Chang, H. J. Kimble, and J. I. Cirac, Deterministic Generation of Arbitrary Photonic States Assisted by Dissipation, Phys. Rev. Lett. **115**, 163603 (2015).

[78] G. L. Sewell, *Irreversible Quantum Dynamics* (Springer-Verlag, Berlin/Heidelberg, 2003).

[79] C. K. Law and J. H. Eberly, Arbitrary Control of a Quantum Electromagnetic Field, Phys. Rev. Lett. **76**, 1055 (1996).

[80] V. S. C. Manga Rao and S. Hughes, Single quantum-dot Purcell factor and β factor in a photonic crystal waveguide, Phys. Rev. B **75**, 205437 (2007).

[81] M. C. Kuzyk and H. Wang, Scaling Phononic Quantum Networks of Solid-State Spins with Closed Mechanical Subsystems, Phys. Rev. X **8**, 041027 (2018).

[82] W. M. Itano, D. J. Heinzen, J. J. Bollinger, and D. J. Wineland, Quantum Zeno effect, Phys. Rev. A **41**, 2295 (1990).

[83] S. Maniscalco, F. Francica, R. L. Zaffino, N. Lo Gullo, and F. Plastina, Protecting Entanglement via the Quantum Zeno Effect, Phys. Rev. Lett. **100**, 090503 (2008).

[84] Y. Li, X. Chen, and M. P. A. Fisher, Quantum Zeno effect and the many-body entanglement transition, Phys. Rev. B **98**, 205136 (2018).

[85] P. Facchi and S. Pascazio, Quantum Zeno Subspaces, Phys. Rev. Lett. **89**, 080401 (2002).

[86] M. Zhang and L. You, Quantum Zeno Subspace and Entangled Bose-Einstein Condensates, Phys. Rev. Lett. **91**, 230404 (2003).

[87] A. Beige, D. Braun, B. Tregenna, and P. L. Knight, Quantum Computing Using Dissipation to Remain in a Decoherence-Free Subspace, Phys. Rev. Lett. **85**, 1762 (2000).

[88] S.-Y. Bai and J.-H. An, Generating Stable Spin Squeezing by Squeezed-Reservoir Engineering, Phys. Rev. Lett. **127**, 083602 (2021).

[89] J. Wang, Y. Zhou, X. Zhang, F. Liu, Y. Li, K. Li, Z. Liu, G. Wang, and W. Gao, Efficient Generation of an Array of Single Silicon-Vacancy Defects in Silicon Carbide, Phys. Rev. Appl. **7**, 064021 (2017).

[90] D. M. Toyli, C. D. Weis, G. D. Fuchs, T. Schenkel, and D. D. Awschalom, Chip-scale nanofabrication of single spins and spin arrays in diamond, Nano Lett. **10**, 3168 (2010).

[91] J. Nogueira, P. A. Oliveira, F. M. Souza, and L. Sanz, Dynamic generation of Greenberger-Horne-Zeilinger states with coupled charge qubits, Phys. Rev. A **103**, 032438 (2021).